

Ramsey interferometry through coherent $X^2\Sigma_g^+ - A^2\Pi_u - B^2\Sigma_u^+$ coupling and population transfer in N_2^+ air laser

Yu-Hung Kuan,¹ Xiangxu Mu,² Zhiming Miao,² Wen-Te Liao,^{1,*} Chengyin Wu,² and Zheng Li^{2,†}

¹*Department of Physics, National Central University, Taoyuan City 32001, Taiwan*

²*State Key Laboratory for Mesoscopic Physics, School of Physics, Peking University, Beijing 100871, Peoples Republic of China*

(Dated: June 16, 2020)

The laser-like coherent emission at 391nm from N_2 gas irradiated by strong 800nm pump laser and weak 400nm seed laser is theoretically investigated. Recent experimental observations are well simulated, including temporal profile, optical gain and periodic modulation of the 391nm signal from N_2^+ . Our calculation sheds light on the long standing controversy on whether population inversion is indispensable for the optical gain. We demonstrate the Ramsey interference fringes of the emission intensity at 391nm formed by additionally injecting another 800nm pump or 400nm seed, which are well explained by the coherent modulation of transition dipole moment and population between the $A^2\Pi_u(\nu = 2) - X^2\Sigma_g^+$ states as well as the $B^2\Sigma_u^+(\nu = 0) - X^2\Sigma_g^+$ states. This study provides versatile possibilities for the coherent control of N_2^+ air laser.

PACS numbers: 42.50.-p, 33.20.t, 34.10.+x

Keywords: N_2^+ air laser, Ramsey interference, coherent control

A plasma filamentation will be formed when strong femtosecond laser pulses propagate in air, in which Yao et al. [1] firstly reported the directional narrow-band emissions from singly ionized nitrogen molecules. This kind of mirror-free coherent emission of ambient air has potential application in remote sensing and has attracted great interest. The generation of the coherent emission around 391 nm, corresponding to the transition of N_2^+ ($B^2\Sigma_u^+, \nu'' = 0 \rightarrow X^2\Sigma_g^+, \nu = 0$), has been extensively investigated[2–16]. The underlying mechanism is much more complicated when the pump laser wavelength is around 800 nm [10]. The strong laser field will cause coherent coupling of the electronic, vibrational, and rotational freedom of the ionized nitrogen molecules. The coherent emission around 391 nm can be amplified by two or three orders of magnitude when injecting a seed laser with spectrum covering 391 nm. Further it is found that the amplified emission lags behind the seed for several picoseconds and lasts tens of picoseconds. The amplified coherent emission is triggered in a pencil-like sample, as the macroscopic polarization is established by the seed, the effect is experimentally identified as superfluorescence [2, 14, 15]. Even though partial evidences support the establishment of population inversion between N_2^+ ($B^2\Sigma_u^+, \nu'' = 0$) and N_2^+ ($X^2\Sigma_g^+, \nu = 0$) by the 800 nm pump laser, it is still under hot debate whether population inversion is indispensable for the optical gain because superfluorescence could in principle be formed without population inversion. The post-ionization population redistribution mechanism (PPRM) is proposed to interpret the establishment of the population inversion[4, 16], in which the population is transferred from N_2^+ ($X^2\Sigma_g^+$) to N_2^+ ($A^2\Pi_u$) by the 800 nm pump laser. The population redistribution helps to build the population inversion between N_2^+ ($B^2\Sigma_u^+, \nu'' = 0$) and N_2^+ ($X^2\Sigma_g^+, \nu = 0$). Very recently, the crucial involve-

ment of the N_2^+ ($A^2\Pi_u$) state in the lasing process is verified in the experiments with 800nm pump field[8, 9, 13]. Further, some periodic modulations of the 391nm coherent emission are observed in experiments by double-seed and double-pump schemes [14, 15].

Here we provide theoretical study of effects of $A^2\Pi_u(\nu = 0, 1, 2)$ state to the 391 nm optical gain based on the double-pump-seed scheme, and coherence effects induced by pair of seed pulses based on pump-double-seed scheme. We also focus on the population evolution induced by the 800nm pump pulse, and its consequences to the 391nm emission. The energy level diagram of the mixed $N_2-N_2^+$ system is shown in Fig. 1(a), where we include three vibrational states of $A^2\Pi_u$, labeled as |2>, |3>, |4>. The $X^2\Sigma_g^+ - A^2\Pi_u(\nu = 2)$ transition is resonant with the 800nm pump and the second weak pump pulse, which has a spectral range from 770nm to 830nm. In Fig 1(b), we show the pulse sequences of the double pump-seed and the pump-double seed schemes. Superfluorescence emission around 391 nm corresponding to the transition from $B^2\Sigma_u^+(\nu = 0)$ to $X^2\Sigma_g^+$ state is generated when a delayed seed laser is injected into the ionized nitrogen gas. Ramsey fringes [17] show up in two following cases: (1) when another 391nm seed laser is injected and scanned over the relative delay $T_s + \tau_{ss}$ between the two seed pulses (see Fig. 1(b)); (2) alternatively, shining another 800nm pump pulse and scanning over the temporal spacing $T_p + \tau_{pp}$ between the two pump pulses (see Fig. 1(c)). The major time delays $T_p = 1.5$ ps and $T_s = 3$ ps are introduced, in order to make the pairs of pump and seed pulses temporally separated, in this way, we can exclude the fringes formed by the direct interference of temporally overlapping pulse pairs. The experimental observation of Ramsey interference fringes at 391nm emission intensity modulation as a function of τ_{pp} and with a period of 2.6fs corresponding to the transition frequency between the $A^2\Pi_u(\nu = 2) - X^2\Sigma_g^+$ states[15] suggests that $A^2\Pi_u(\nu = 2)$ and $X^2\Sigma_g^+$ are coherently populated by the pump laser, and it also provides a direct route to control the

*Electronic address: wente.liao@nctu.edu.tw

†Electronic address: zheng.li@pku.edu.cn

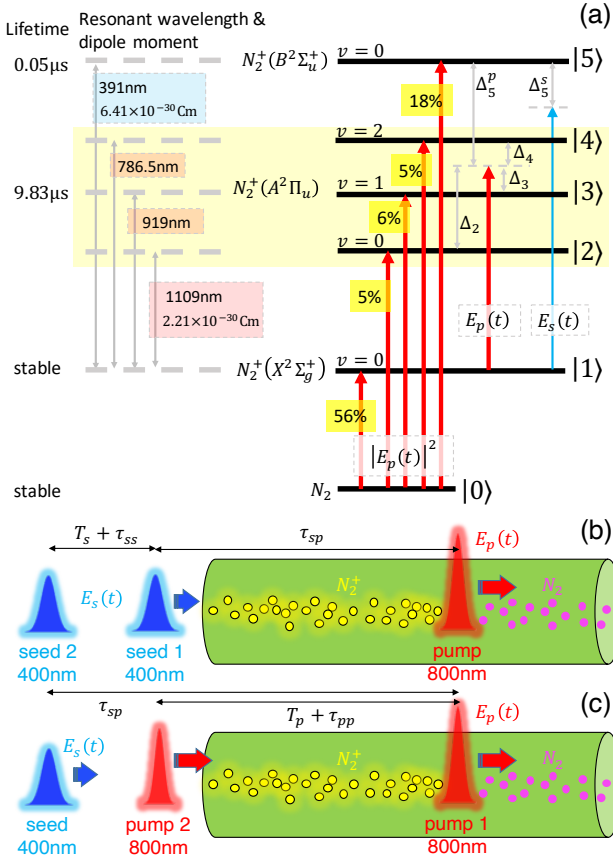


FIG. 1: (Color online) (a) N_2^+ level scheme. A 800nm pump pulse E_p (red upward arrow) simultaneously ionizes N_2 , with corresponding branching ratio indicated by yellow-background percentages, and coherently drives N_2^+ transitions with detunings $\Delta_2, \Delta_3, \Delta_4$ and Δ_5^p , respectively. A 400nm seed pulse E_s (blue upward arrow) drives transition $|1\rangle \rightarrow |5\rangle$ with detuning Δ_5^s and induces emission at wavelength 391nm. (b) double-seed (blue Gaussians) and one pump pulse (red Gaussian) scheme. Red and yellow dots depict N_2 and N_2^+ , respectively. τ_{sp} and $T_s + \tau_{ss}$ are delay time between the pump pulse and the first seed pulse and that between two seed pulses, respectively. (c) one seed and double-pump pulses scheme. $T_p + \tau_{pp}$ is the delay time between two pump pulses.

391nm $B^2\Sigma_u^+(\nu = 0) - X^2\Sigma_g^+$ emission by manipulating the $A^2\Pi_u(\nu = 2) - X^2\Sigma_g^+$ coherence.

We simulate the N_2^+ air lasing process by employing the semiclassical optical-Bloch equation [18–20]. As demonstrated in Fig. 1, a strong 800nm pump pulse propagates through a gas composed of nitrogen molecules, which does not only ionizes certain amount of neutral N_2 in the initial state $|0\rangle$, but also coherently drives population transfer among five involved levels of N_2^+ cation, namely, PPRM. Via PPRM the population among N_2^+ levels is redistributed, and especially, significant amount of population is depleted from state $|1\rangle$ and transferred to high energy levels $|2\rangle, |3\rangle$ and $|4\rangle$ in the $A^2\Pi_u$ manifold. When the population of state $|5\rangle$ dominates over that of $|1\rangle$ due to PPRM, the cloud of N_2^+ becomes a pencil-like active medium as in the experiment [14, 15]. Subsequently, a 400nm seed pulse illuminates the population-

inverted N_2^+ gas and stimulates the emission from $|5\rangle \rightarrow |1\rangle$ transition. The coupled optical-Bloch equation [18–23] is used to describe our system.

$$\partial_t \hat{\rho} = \frac{1}{i\hbar} [\hat{H}, \hat{\rho}] + \hat{T} + \mathcal{L}\rho, \quad (1)$$

$$\frac{1}{c} \partial_t E_p + \partial_z E_p = i \frac{2\pi n}{\epsilon_0} \left(\frac{P_A}{\lambda_{21}} \rho_{21} + \frac{P_A}{\lambda_{31}} \rho_{31} + \frac{P_A}{\lambda_{41}} \rho_{41} + \frac{P_B}{\lambda_{51}} \rho_{51}^p \right), \quad (2)$$

$$\frac{1}{c} \partial_t E_s + \partial_z E_s = i \frac{2\pi n}{\epsilon_0} \frac{P_B}{\lambda_{51}} \rho_{51}^s, \quad (3)$$

with initial and boundary conditions

$$\rho_{ij}(0, z) = \delta_{i0} \delta_{j0}, \quad (4)$$

$$E_p(0, z) = E_s(0, z) = 0, \quad (5)$$

$$E_p(t, 0) = E_{p1} \exp \left[- \left(\frac{t - \tau_{p1}}{\sqrt{2}\tau} \right)^2 \right] + E_{p2} \exp \left[- \left(\frac{t - \tau_{p2}}{\sqrt{2}\tau} \right)^2 + i\omega_p (T_p + \tau_{pp}) \right], \quad (6)$$

$$E_s(t, 0) = E_{s1} \exp \left[- \left(\frac{t - \tau_{s1}}{\sqrt{2}\tau} \right)^2 \right] + E_{s2} \exp \left[- \left(\frac{t - \tau_{s2}}{\sqrt{2}\tau} \right)^2 + i\omega_s (T_s + \tau_{ss}) \right], \quad (7)$$

where δ_{ij} is the Kronecker delta symbol. $\hat{\rho}$ is the density matrix of the five-level system in Fig. 1(a), and \hat{H} is the laser-molecular coupling Hamiltonian. $\hat{T} = W_0 \rho_{00}(t) \exp \left[- \frac{2(2I_p)^{3/2}}{3E_p(t)} \left(\frac{\sqrt{m}}{e\hbar} \right) \right] \sum_{i,j} F_{ij} |i\rangle \langle j|$ characterizes the tunneling ionization rate based on the ADK formula [24]. W_0 the tunnelling ionization rate determined from the condition $\int_{-\infty}^{\infty} \hat{T}_{00} dt = 0.9$ based on experimental observation [16]. F_{ii} are the branching ratio of the N_2^+ states and are defined as

$$F_{ii}^A = \left| \langle \phi_{vi}(A(N_2^+)) | \psi_0(X(N_2)) \rangle \right|^2, \quad (8)$$

$$F_{ii}^B = \left| \langle \phi_{vi}(B(N_2^+)) | \psi_0(X(N_2)) \rangle \right|^2. \quad (9)$$

In order to determine F_{ii} , we solve Schrödinger equation based on discrete variable representation and ab initio potential [16] and obtain $F_{00} = -1$, $F_{11} = 0.55825$, $F_{22} = 0.05305$, $F_{33} = 0.06259$, $F_{44} = 0.05202$, $F_{55} = 0.17885$. (see details in Supplementary Material). $E_{p(s)}$ is the slowly varying envelope of pump (seed) laser electric field. $\mathcal{L}\rho$ effectively characterizes the spontaneous decay and other decoherence processes. Especially, $\mathcal{L}\rho_{41} = -\Gamma/2 - \Gamma_a/2$ and $\mathcal{L}\rho_{51} = -\Gamma/2 - \Gamma_b/2$. ρ_{41} and $\rho_{51}^{(s)}$ represent the coherence of transition $|1\rangle \rightarrow |4\rangle$ and $|1\rangle \rightarrow |5\rangle$ driven by pump (seed) laser respectively. The complete optical-Bloch equation and the simulation parameters are elaborated in the Supplementary Material. The emission spectrum is calculated by

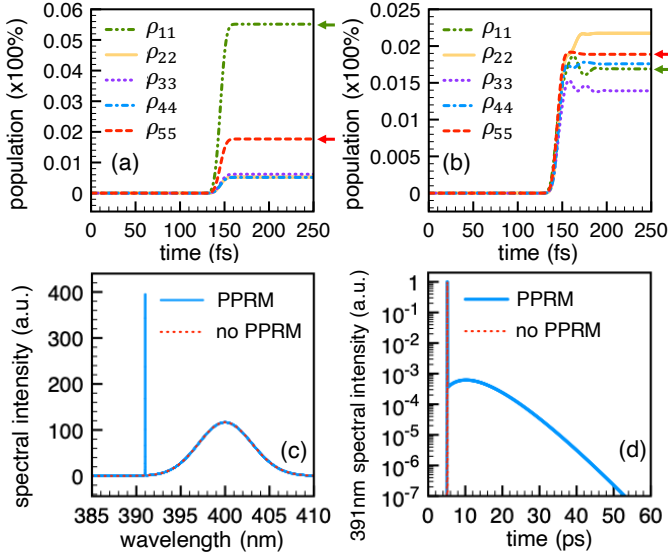


FIG. 2: (Color online) Population dynamics induced by pump pulse (a) without PPRM, (b) with PPRM. Green and red leftward arrows indicate ρ_{11} and ρ_{55} , respectively. (c) The output spectra and (d) temporal evolution of the output spectral intensity at 391nm with (blue-solid line) and without (red-dotted line) PPRM.

the Fourier transformation of the output seed pulse at $z = L$, namely,

$$S(\Delta) = \left| \int_{-\infty}^{\infty} E_s(t, L) e^{-i\Delta t} dt \right|^2, \quad (10)$$

In order to prove the proposed PPRM mechanism, we demonstrate the pump-pulse induced dynamics of N_2^+ population without and with PPRM in Fig. 2(a) and (b), respectively. In Fig. 2(a), all resulting population from mere ionization is given by the branching ratio F_{ii} , and especially there is no population inversion between state $|5\rangle$ and $|1\rangle$. However, when PPRM is included, the population inversion condition $\rho_{55} - \rho_{11} > 0$ is significantly observed in the presence of the pump pulse (see red-dashed and green-dashed-dot lines in Fig. 2(b)), which may play the key role to air lasing at 391nm. For this reason, in the output spectra shown in Fig. 2(c), strong 391nm emission line emerges accompanying the PPRM process. Employing the continuous wavelet transform (CWT) [25], we extract the temporal evolution of the 391nm spectral intensity (see details in Supplementary Material). As illustrated in Fig. 2(d), the 391nm emission under PPRM condition clearly demonstrates the dynamical establishment and decay of the macroscopic polarization on a 10-picosecond time scale. Our calculations reproduced previous experimental observations [2, 14, 15], in which the coherent 391nm emission is identified as superfluorescence. To prove the population inversion is indispensable for the optical gain at 391nm, we simulate the process zero ionization rate of $B^2\Sigma_u^+(\nu = 0)$ (state $|5\rangle$). In Fig. 3(a), the temporal evolution of the seed laser shows modulation in form of a Bessel function [26]. Because the ionization rate of state $|5\rangle$ is assumed to be zero, the population of state $|5\rangle$ can just grow by PPRM. From the above assumption, no population inversion

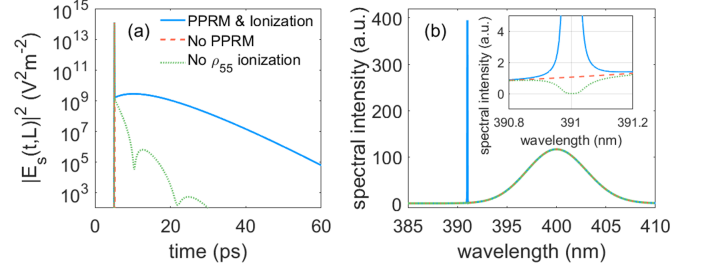


FIG. 3: (Color online) Dynamics without population inversion. (a) Temporal evolution of the seed laser. (b) Output spectra with the assumption that no PPRM or no ionization in $B^2\Sigma_u^+(\nu = 0)$ (setting $F_{55} = 0$ for state $|5\rangle$) is present. Two figures share the same legend.

is present, so the photons with 391nm wavelength will be absorbed (see Fig. 3(b)), namely, there is no optical gain but an absorption dip in the output spectra.

In order to demonstrate the build-up dynamics of coherence and population inversion between state $|5\rangle$ and $|1\rangle$, we simulate the Ramsey fringes by subsequently illuminating the N_2^+ medium with two seed pulses spaced out adjustable time delay $T_s + \tau_{ss}$ apart, where the major delay $T_s = 3ps$ excludes the interference of overlapping light field. Fig. 4 shows the τ_{ss} -dependent spectral intensity $S(\Delta)$, and the interference fringes clearly reveal the coherence between $B^2\Sigma_u^+(\nu = 0)$ and $X^2\Sigma_g^+$ states. And the modulation with 1.3fs period in Fig. 4 originates from the interference of the coherence of $|1\rangle \rightarrow |5\rangle$ transition pre-constructed by the first seed pulse and the second seed pulse, which is consistent with observations [14]. To further investigate the effect of double-seed scheme on N_2^+ dynamics, Fig. 4(b) and Fig. 4(c) illustrate the degrees of polarization and population inversion of the $B^2\Sigma_u^+(\nu = 0)$ and $X^2\Sigma_g^+$ states, characterized by the maximum density matrix elements ρ_{51} and $\rho_{55} - \rho_{11}$ normalized to their corresponding single seed results. The Ramsey interference period of 1.3fs corresponds to the transition frequency between $X^2\Sigma_g^+$ and $B^2\Sigma_u^+(\nu = 0)$ states, the interference fringes are in phase with the oscillation of polarization. The degree of population inversion in Fig. 4(c) oscillates out of phase to the 391nm spectral intensity oscillation by half a period, as the stronger emission of 391nm photons weakens the degree of population inversion. It is clear from Fig. 4 that the amplitude of polarization oscillation is 2 orders of degree larger than that of the population inversion degree, this fact unambiguously demonstrates the dominance of coherence in altering the intensity of superfluorescence emission, despite of the indispensable requirement of population inversion between $B^2\Sigma_u^+(\nu = 0)$ and $X^2\Sigma_g^+$ states in the N_2^+ system. It paves the way to devise novel method for coherent control of the N_2^+ air laser emission.

Fig. 5(a) shows the 391nm signal intensity as a function of the time delay $T_p + \tau_{pp}$ between the two 800nm pump pulses with the major delay $T_p = 1.5ps$, and $\tau_{sp} = 5ps$, the second pump pulse is injected between the first pump and the seed pulses. The period of modulation is about 2.6fs and corresponds to the transition frequency between state $A^2\Pi_u(\nu = 2)$ and state $X^2\Sigma_g^+$. We further demonstrate the effect of the second pump pulse on the coherence in Fig. 5(b) as well as

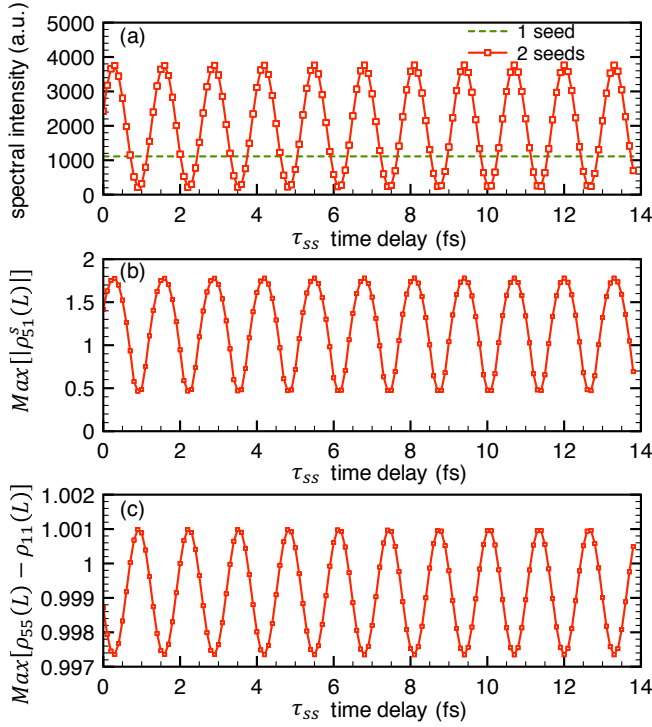


FIG. 4: (Color online) (a) τ_{ss} -dependent spectral intensity at 391nm. Red solid line (green dashed line) is the intensity induced by two separated seed pulses (only one seed pulse). The major delay time between the two seed pulses is $T_s = 3\text{ps}$ and the pump-seed delay is $\tau_{sp} = 0.1\text{ps}$. The corresponding (b) maximum $|\rho_{51}^s(L)|$ and (c) maximum inversion $\rho_{55}(L) - \rho_{11}(L)$, normalized to single-seed result, are demonstrated.

the population inversion of $B^2\Sigma_u^+(\nu = 0) - X^2\Sigma_g^+$ state in Fig. 5(c). We normalize the polarization and population inversion degree between $B^2\Sigma_u^+(\nu = 0)$ and $X^2\Sigma_g^+$ with their values of the single-pump scheme. For the Ramsey interference in the double pump scheme, the amplitude of oscillation of the population inversion degree becomes significantly larger and is on the same order of magnitude as the oscillation amplitude of the polarization Fig.5(b)(c)). Besides, it is in phase with the intensity oscillation. This signature indicates that the population ρ_{11} of the ground state $X^2\Sigma_g^+$ is strongly modulated by the second 800nm pump laser with the angular frequency of $2\pi c/800\text{nm}$. It is a direct consequence from the fact that the $A^2\Pi_u(\nu = 2)$ and $X^2\Sigma_g^+$ must be coherently populated by the pump laser, and is consistent with coherent population transfer of the PPRM mechanism. The double pump scheme can thus provide strong evidence for the coherent nature of the air laser, and exclusion of any description based on traditional laser rate equations. Fig.5(b) demonstrates strong dependence of 391nm emission intensity on the $B^2\Sigma_u^+(\nu = 0) - X^2\Sigma_g^+$ polarization, which is induced by the 400nm seed pulse.

We have studied the coherence driven superfluorescence of the N_2^+ air laser system, and have demonstrated the coherence between the $A^2\Pi_u(\nu = 2) - X^2\Sigma_g^+$ as well as the $B^2\Sigma_u^+(\nu = 0) - A^2\Pi_u(\nu = 2)$ pairs employing the Ramsey

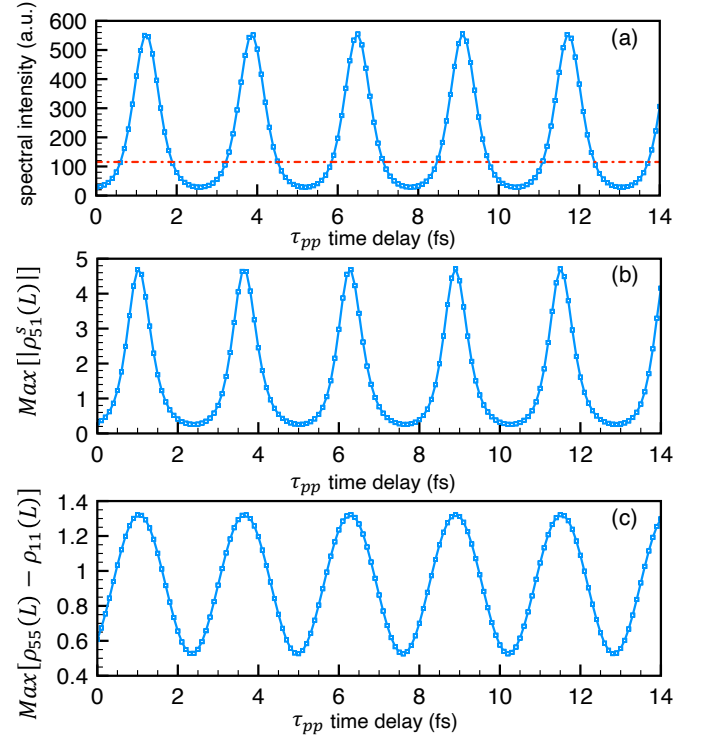


FIG. 5: (Color online) (a) the spectral interference fringes at 391nm, (b) maximum $|\rho_{51}^s(L)|$ and, (c) maximum $\rho_{55}(L) - \rho_{11}(L)$ are illustrated. The latter two quantities are normalized to their single pump result. The red dashed dotted line depicts the corresponding spectral intensity for cases with only one pump pulse.

interferometry in the temporal domain. In the Ramsey interferometry, additional weak pulses of 800nm and 400nm wavelengths are injected and scanned over their relative time delays with respect to the major pump and seed pulses, which are resonant with the $A^2\Pi_u(\nu = 2) - X^2\Sigma_g^+$ (800nm) and $B^2\Sigma_u^+(\nu = 0) - X^2\Sigma_g^+$ (400nm) transitions. The resulting Ramsey interference fringes, i.e. the 2.6fs and 1.3fs periodic oscillations in the intensity of 391nm emission from $B^2\Sigma_u^+(\nu = 0)$ to $X^2\Sigma_g^+$ transition as functions of relative delays between the two pump and the two seed pulses, have clearly illustrated the coherent population transfer and modulation of $B^2\Sigma_u^+(\nu = 0) - X^2\Sigma_g^+$ polarization in the $X^2\Sigma_g^+ - A^2\Pi_u - B^2\Sigma_u^+$ system. Interestingly, although the double-seed scheme (Fig. 4) and double-pump scheme (Fig. 5) can both enhance the 391nm emission, they are subject to different mechanisms, and thus provides variety of possibilities for the coherent control of the N_2^+ air laser. While lasing with two 391nm seed pulses, the $B^2\Sigma_u^+(\nu = 0) - X^2\Sigma_g^+$ polarization has dominant contribution to the 391nm emission, the lasing with two 800nm pump pulses strongly relies on the degrees of both population inversion as well as polarization. In the double-pump scheme, the second weak 800nm pump pulse tunes the $A^2\Pi_u(\nu = 2) - X^2\Sigma_g^+$ coherence, and then indirectly affects the emission from $B^2\Sigma_u^+(\nu = 0)$ to $X^2\Sigma_g^+$ state transition, it enriches the understanding of the coherence relations of the $X^2\Sigma_g^+ - A^2\Pi_u - B^2\Sigma_u^+$ system as a

complete picture, and shows that the superfluorescence emitted from $B^2\Sigma_u^+(\nu = 0)$ to $X^2\Sigma_g^+$ transition can be coherently controlled by the transfer between the $A^2\Pi_u(\nu = 2)$ and $X^2\Sigma_g^+$ state. The consistency of the theory with forward lasing experiment[15] sets the investigation of the backward lasing in the N_2^+ system on a solid basis, which is suppressed by still unknown mechanisms and has not yet been experimentally realized.

Y.-H. K. and W.-T. L. are supported by the Ministry of Science and Technology, Taiwan (Grant No. MOST 107-2112-M-008-007-MY3 and Grant No. MOST 107-2745-M-007-001-). W.-T. L. is also supported by the National Center for Theoretical Sciences, Taiwan. C. W. would like to acknowledge the support from the National Natural Science Foundation of China (Grant Nos. 11625414 and 21673006).

Appendix A: The optical-Bloch equations and simulation parameters

In the following we present the complete optical-Bloch equations [27] and detail of our simulation parameters for the N_2^+ air laser system and the Ramsey fringes [17]. The Hamiltonian reads $\hat{H} = \hat{H}_0 + \hat{H}_I$, where

$$\hat{H}_0 = \hbar\omega_2|2\rangle\langle 2| + \hbar(\omega_2 + v_1)|3\rangle\langle 3| + \hbar(\omega_2 + v_2)|4\rangle\langle 4| + \hbar\omega_3|5\rangle\langle 5|, \quad (A1)$$

$$\hat{H}_I = -\frac{\hbar}{2}\Omega_p e^{-i(\omega_p t - k_p z)} (|2\rangle\langle 1| + |3\rangle\langle 1| + |4\rangle\langle 1|) - \frac{\hbar}{2} \left(\Omega_f e^{-i(\omega_p t - k_p z)} + \Omega_s e^{-i(\omega_s t - k_s z)} \right) |5\rangle\langle 1| + H.c.. \quad (A2)$$

Together with the transformations $\rho_{21} \rightarrow e^{-i(\omega_p t - k_p z)} \rho_{21}$, $\rho_{31} \rightarrow e^{-i(\omega_p t - k_p z)} \rho_{31}$, $\rho_{41} \rightarrow e^{-i(\omega_p t - k_p z)} \rho_{41}$, $\rho_{51} \rightarrow e^{-i(\omega_s t - k_s z)} \rho_{51s} + e^{-i(\omega_p t - k_p z)} \rho_{51p}$, $\rho_{52} \rightarrow e^{-i(\omega_s t - \omega_p t - k_s z + k_p z)} \rho_{52s} + \rho_{52p}$, $\rho_{53} \rightarrow e^{-i(\omega_s t - \omega_p t - k_s z + k_p z)} \rho_{53s} + \rho_{53p}$, and $\rho_{54} \rightarrow e^{-i(\omega_s t - \omega_p t - k_s z + k_p z)} \rho_{54s} + \rho_{54p}$, one can expand $\partial_t \hat{\rho} = \frac{1}{i\hbar} [\hat{H}, \hat{\rho}] + \hat{T} + \mathcal{L}\rho$ and gets

$$\begin{aligned} \frac{\partial \rho_{11}}{\partial t} &= F_{11} w_0 \rho_0 \exp \left[-\frac{2(2I_p)^{\frac{3}{2}} \sqrt{m}}{3E_p q_e \hbar} \right] + \Gamma_b \rho_{55} + \Gamma_a \rho_{44} + \Gamma_a \rho_{33} + \Gamma_a \rho_{22} \\ &+ \frac{i}{2} [\Omega_p^* \rho_{21} + \Omega_p^* \rho_{31} + \Omega_p^* \rho_{41} + \Omega_f^* \rho_{51p} + \Omega_s^* \rho_{51s} - \rho_{51p}^* \Omega_f - \rho_{21}^* \Omega_p - \rho_{31}^* \Omega_p \\ &- \rho_{41}^* \Omega_p - \rho_{51s}^* \Omega_s] + e^{i(\omega_p - \omega_s)t} (\Omega_f^* \rho_{51s} - \rho_{51p}^* \Omega_s) + e^{-i(\omega_p - \omega_s)t} (\Omega_s^* \rho_{51p} - \rho_{51s}^* \Omega_f), \end{aligned} \quad (A3)$$

$$\frac{\partial \rho_{22}}{\partial t} = F_{22} w_0 \rho_0 \exp \left[-\frac{2(2I_p)^{\frac{3}{2}} \sqrt{m}}{3E_p q_e \hbar} \right] - \Gamma_a \rho_{22} + \frac{i}{2} (\rho_{21}^* \Omega_p - \rho_{21} \Omega_p^*), \quad (A4)$$

$$\frac{\partial \rho_{33}}{\partial t} = F_{33} w_0 \rho_0 \exp \left[-\frac{2(2I_p)^{\frac{3}{2}} \sqrt{m}}{3E_p q_e \hbar} \right] - \Gamma_a \rho_{33} + \frac{i}{2} (\rho_{31}^* \Omega_p - \rho_{31} \Omega_p^*), \quad (A5)$$

$$\frac{\partial \rho_{44}}{\partial t} = F_{44} w_0 \rho_0 \exp \left[-\frac{2(2I_p)^{\frac{3}{2}} \sqrt{m}}{3E_p q_e \hbar} \right] - \Gamma_a \rho_{44} + \frac{i}{2} (\rho_{41}^* \Omega_p - \rho_{41} \Omega_p^*), \quad (A6)$$

$$\begin{aligned} \frac{\partial \rho_{55}}{\partial t} &= F_{55} w_0 \rho_0 \exp \left[-\frac{2(2I_p)^{\frac{3}{2}} \sqrt{m}}{3E_p q_e \hbar} \right] - \Gamma_b \rho_{55} \\ &- \frac{i}{2} \left[\Omega_f^* \rho_{51p} + \Omega_s^* \rho_{51s} - \rho_{51p}^* \Omega_f - \rho_{51s}^* \Omega_s + e^{i(\omega_p - \omega_s)t} (\Omega_f^* \rho_{51s} - \rho_{51p}^* \Omega_s) + e^{-i(\omega_p - \omega_s)t} (\Omega_s^* \rho_{51p} - \rho_{51s}^* \Omega_f) \right], \end{aligned} \quad (A7)$$

$$\begin{aligned} \frac{\partial \rho_{21}}{\partial t} &= -\frac{\Gamma_a}{2} \rho_{21} \\ &- \frac{i}{2} \left[\Omega_p (\rho_{32}^* + \rho_{42}^* - \rho_{11} + \rho_{22}) + \rho_{52p}^* (\Omega_f + \Omega_s e^{it(\omega_p - \omega_s)}) + \rho_{52s}^* (\Omega_s + \Omega_f e^{-it(\omega_p - \omega_s)}) + 2\rho_{21}(\omega_2 - \omega_p) \right], \end{aligned} \quad (A8)$$

$$\frac{\partial \rho_{32}}{\partial t} = -\Gamma_a \rho_{32} - \frac{i}{2} (-\Omega_p \rho_{21}^* + \rho_{31} \Omega_p^* + 2\rho_{32} v_1), \quad (A9)$$

$$\begin{aligned} \frac{\partial \rho_{31}}{\partial t} &= -\frac{\Gamma_a}{2} \rho_{31} \\ &\quad -\frac{i}{2} \left[\Omega_p (\rho_{43}^* - \rho_{11} + \rho_{32} + \rho_{33}) + \rho_{53p}^* (\Omega_f + \Omega_s e^{it(\omega_p - \omega_s)}) + \rho_{53s}^* (\Omega_s + \Omega_f e^{-it(\omega_p - \omega_s)}) + 2\rho_{31}(v_1 + \omega_2 - \omega_p) \right], \end{aligned} \quad (\text{A10})$$

$$\begin{aligned} \frac{\partial \rho_{41}}{\partial t} &= -\left(\frac{\Gamma_a}{2} + \gamma_{41} \right) \rho_{41} \\ &\quad -\frac{i}{2} \left[\rho_{54p}^* (\Omega_f + \Omega_s e^{it(\omega_p - \omega_s)}) + \rho_{54s}^* (\Omega_s + \Omega_f e^{-it(\omega_p - \omega_s)}) + \Omega_p (-\rho_{11} + \rho_{42} + \rho_{43} + \rho_{44}) + 2\rho_{41}(v_2 + \omega_2 - \omega_p) \right], \end{aligned} \quad (\text{A11})$$

$$\frac{\partial \rho_{42}}{\partial t} = -\Gamma_a \rho_{42} - \frac{i}{2} (2v_2 \rho_{42} - \Omega_p \rho_{21}^* + \rho_{41} \Omega_p^*), \quad (\text{A12})$$

$$\frac{\partial \rho_{43}}{\partial t} = -\Gamma_a \rho_{43} + \frac{i}{2} [2(v_1 - v_2) \rho_{43} + \Omega_p \rho_{31}^* - \rho_{41} \Omega_p^*], \quad (\text{A13})$$

$$\frac{\partial \rho_{51s}}{\partial t} = -\left(\frac{\Gamma_b}{2} + \Gamma \right) \rho_{51s} - \frac{i}{2} [\Omega_s (\rho_{55} - \rho_{11}) + 2(\omega_3 - \omega_s) \rho_{51s} + \Omega_p (\rho_{52s} + \rho_{53s} + \rho_{54s})], \quad (\text{A14})$$

$$\frac{\partial \rho_{51p}}{\partial t} = -\left(\frac{\Gamma_b}{2} + \Gamma \right) \rho_{51p} - \frac{i}{2} [\Omega_f (\rho_{55} - \rho_{11}) + 2\rho_{51p}(\omega_3 - \omega_p) + \rho_{52p} \Omega_p + \Omega_p (\rho_{53p} + \rho_{54p})], \quad (\text{A15})$$

$$\frac{\partial \rho_{52s}}{\partial t} = -\left(\frac{\Gamma_a + \Gamma_b}{2} + \Gamma \right) \rho_{52s} + \frac{i}{2} [2(\omega_2 - \omega_3 - \omega_p + \omega_s) \rho_{52s} + \Omega_s \rho_{21}^* - \rho_{51s} \Omega_p^*], \quad (\text{A16})$$

$$\frac{\partial \rho_{52p}}{\partial t} = -\left(\frac{\Gamma_a + \Gamma_b}{2} + \Gamma \right) \rho_{52p} - \frac{i}{2} [2(\omega_3 - \omega_2) \rho_{52p} - \Omega_f \rho_{21}^* + \rho_{51p} \Omega_p^*], \quad (\text{A17})$$

$$\frac{\partial \rho_{53s}}{\partial t} = -\left(\frac{\Gamma_a + \Gamma_b}{2} + \Gamma \right) \rho_{53s} + \frac{i}{2} [2(v_1 + \omega_2 - \omega_3 - \omega_p + \omega_s) \rho_{53s} + \Omega_s \rho_{31}^* - \rho_{51s} \Omega_p^*], \quad (\text{A18})$$

$$\frac{\partial \rho_{53p}}{\partial t} = -\left(\frac{\Gamma_a + \Gamma_b}{2} + \Gamma \right) \rho_{53p} + \frac{i}{2} [2(v_1 + \omega_2 - \omega_3) \rho_{53p} + \Omega_f \rho_{31}^* - \rho_{51p} \Omega_p^*], \quad (\text{A19})$$

$$\frac{\partial \rho_{54s}}{\partial t} = -\left(\frac{\Gamma_a + \Gamma_b}{2} + \Gamma \right) \rho_{54s} - \frac{i}{2} [-\Omega_s \rho_{41}^* + \rho_{51s} \Omega_s^* - 2\rho_{54s}(v_2 + \omega_2 - \omega_3 - \omega_p + \omega_s)], \quad (\text{A20})$$

$$\frac{\partial \rho_{54p}}{\partial t} = -\left(\frac{\Gamma_a + \Gamma_b}{2} + \Gamma \right) \rho_{54p} + \frac{i}{2} [2(v_2 + \omega_2 - \omega_3) \rho_{54p} + \Omega_f \rho_{41}^* - \rho_{51p} \Omega_p^*], \quad (\text{A21})$$

The wave equations of pump and seed laser pulses read

$$\frac{1}{c} \partial_t E_p + \partial_z E_p = i \frac{2\pi n}{\epsilon_0} \left(\frac{P_A}{\lambda_{21}} \rho_{21} + \frac{P_A}{\lambda_{31}} \rho_{31} + \frac{P_A}{\lambda_{41}} \rho_{41} + \frac{P_B}{\lambda_{51}} \rho_{51p} \right), \quad (\text{A22})$$

$$\frac{1}{c} \partial_t E_s + \partial_z E_s = i \frac{2\pi n}{\epsilon_0} \frac{P_B}{\lambda_{51}} \rho_{51s}. \quad (\text{A23})$$

Together with initial and boundary conditions

$$\rho_{ij}(0, z) = \delta_{i0} \delta_{j0}, \quad (\text{A24})$$

$$E_p(0, z) = 0, \quad (\text{A25})$$

$$E_s(0, z) = 0, \quad (\text{A26})$$

$$\begin{aligned} E_p(t, 0) &= E_{p1} \exp \left[-\left(\frac{t - \tau_{p1}}{\sqrt{2}\tau} \right)^2 \right] \\ &\quad + E_{p2} \exp \left[-\left(\frac{t - \tau_{p2}}{\sqrt{2}\tau} \right)^2 + i\omega_p \tau_{pp} \right], \end{aligned} \quad (\text{A27})$$

$$\begin{aligned} E_s(t, 0) &= E_{s1} \exp \left[-\left(\frac{t - \tau_{s1}}{\sqrt{2}\tau} \right)^2 \right] \\ &\quad + E_{s2} \exp \left[-\left(\frac{t - \tau_{s2}}{\sqrt{2}\tau} \right)^2 + i\omega_s \tau_{ss} \right], \end{aligned} \quad (\text{A28})$$

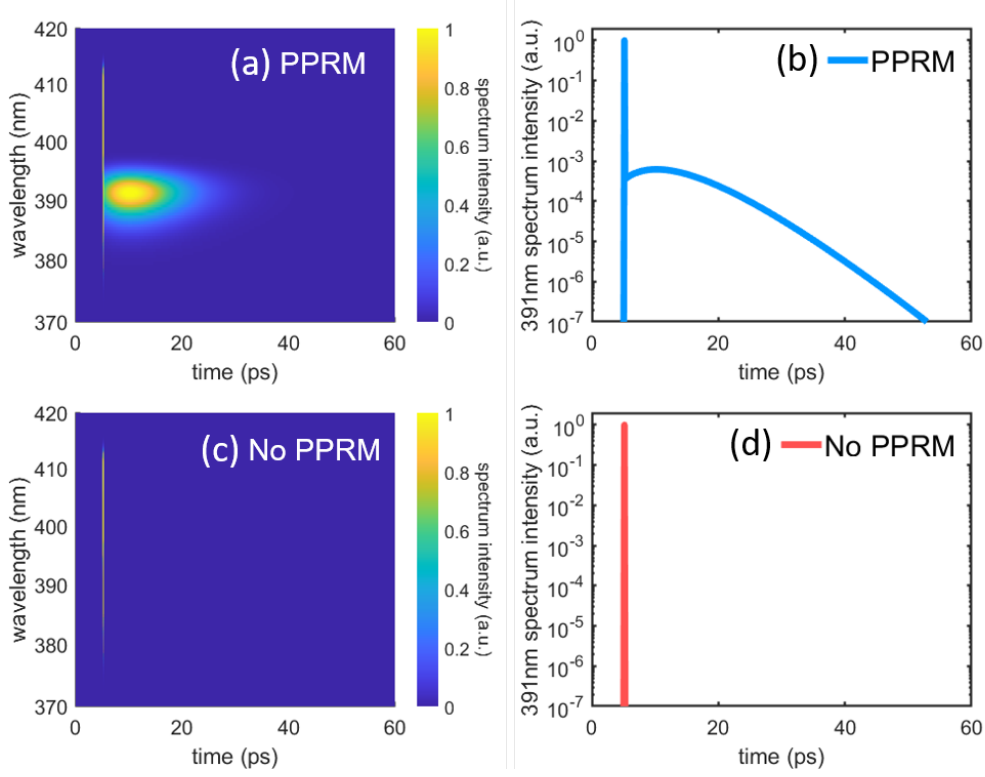


FIG. 6: (a) The continuous wavelet transform (CWT) of the output seed pulse $E_s(t, L)$ with PPRM. (b) The temporal evolution of the 391nm spectral intensity with PPRM. (c) The CWT of the output seed pulse $E_s(t, L)$ without PPRM. (d) The temporal evolution of the 391nm spectral intensity without PPRM.

Because the N_2 molecule is not pre-aligned in space, and the multiphoton ionization does not necessarily produce the $\cos^2 \theta$ distribution along the polarization axis of the ionization laser, given the fact that the outgoing electron is not only in the s -wave state, we can thus assume uniform distribution of the N_2^+ cation in the angular direction. Given the pump and seed pulses have the same linear polarization, the dominant contribution comes from the N_2^+ cation with $\pi/4$ angle between the molecular axis and the laser polarization, and the pump and seed pulses have equal contribution to the vertical $X^2\Sigma_g^+ - A^2\Pi_u$ and parallel $X^2\Sigma_g^+ - B^2\Sigma_u^+(\nu = 0)$ transitions following their selection rules. The numerical methods used for the dynamics of density matrix, namely, Eq. (A3-A21) and the wave equation, i.e., Eq. (A22 & A23), are 4th order Runge-Kutta and Lax method, respectively. Our one-dimensional numerical calculations for the pencil-like N_2 sample are performed in a simulation box $[0, L]$, where laser pulses enter the medium at $z = 0$ and exit at $z = L$. The pulse propagation effects crucially depend on optical depth $n\sigma L$, where n is the particle number density, σ the resonant absorption cross section and L the medium length. For a given optical depth and a σ , no significant difference is observed when varying n and L in the numerical calculation. One thus has flexible choices of n and L for a given $nL = \text{constant}$ to ease the lengthy computation time.

The seed spectra are calculated by

$$S(\Delta) = \left| \int_{-\infty}^{\infty} E_s(t, L) e^{-i\Delta t} dt \right|^2, \quad (\text{A29})$$

namely, the Fourier transformation of the output seed pulses. Here $\Delta = 108.47 \text{ rad}\cdot\text{THz}$ represents the spectral intensity at 391nm. Obtaining the electric field $E_s(t, L)$ of the output seed pulse, we then employ the continuous wavelet transform to analyze the temporal evolution of the key 391nm emission intensity at the lasing wavelength. We use the generalized Morse wavelets with symmetry parameter to be 3 and time-bandwidth product to be 60 [25]. The continuous wavelet analysis of the the output seed pulse is presented in Fig. 6.

TABLE I: Notations used throughout the text.

Notation (unit)	Value	Explanation
c (m/s)	3×10^8	the speed of light in vacuum
ϵ_0 (F/m)	8.85×10^{-12}	vacuum permittivity
\hbar ($\text{m}^2\text{kg/s}$)	1.054×10^{-34}	reduced Planck constant
e (C)	1.602×10^{-19}	electronic charge
m (kg)	9.11×10^{-31}	electronic mass
A_p (W/cm^2)	2.2×10^{14}	peak intensity of pump pulse 1
A_{p2} (W/cm^2)	9.9×10^{11} (Fig. 4)	peak intensity of pump pulse 2
A_s (W/cm^2)	9.259×10^3 (Fig. 3)	peak intensity of seed pulse 1
	5.556×10^4 (Fig. 4)	
A_{s2} (W/cm^2)	9.259×10^3 (Fig. 3)	peak intensity of seed pulse 2
P_A (C · m)	2.21×10^{-30}	dipole moment for transition $X^2\Sigma_g^+ \rightarrow A^2\Pi_u$
P_B (C · m)	6.41×10^{-30}	dipole moment for transition $X^2\Sigma_g^+ \rightarrow B^2\Sigma_u^+$
I_p (eV)	15.58	internal binding energy
n (mm^{-3})	1.237×10^{17}	particle density of N_2 gas
L (mm)	0.01	medium length
Γ (THz)	0.2	collision rate
Γ_a (THz)	2×10^{-5}	decay rate of state $A^2\Pi_u$
Γ_b (THz)	1.017×10^{-7}	decay rate of state $B^2\Sigma_u^+$
τ_{p1} (fs)	113	peak time of pump pulse 1
τ_{pp} (ps)	$-4 - 25$ (Fig. 4)	delay time $\tau_{p2} - \tau_{p1}$
τ_{p2} (ps)	$\tau_{p1} + \tau_{pp}$ (Fig. 4)	peak time of pump pulse 2
τ_{s1} (fs)	213 (Fig. 3)	peak time of seed pulse 1
	5113 (Fig. 4)	
τ_{s2} (fs)	213 – 227 (Fig. 3)	peak time of seed pulse 2
τ_{sp} (ps)	0.1 (Fig. 3)	delay time $\tau_{s1} - \tau_{p1}$
	5 (Fig. 4)	
τ_{ss} (fs)	0 – 14 (Fig. 3)	delay time $\tau_{s2} - \tau_{s1}$
λ_p (nm)	800	central wavelength of pump pulses
λ_s (nm)	400	central wavelength of seed pulses
λ_{21} (nm)	1109	wavelength of transition $ 1\rangle \rightarrow 2\rangle$
λ_{31} (nm)	919	wavelength of transition $ 1\rangle \rightarrow 3\rangle$
λ_{41} (nm)	786.5	wavelength of transition $ 1\rangle \rightarrow 4\rangle$
λ_{51} (nm)	391	wavelength of transition $ 1\rangle \rightarrow 5\rangle$
ω_p (rad/s)	2.36×10^{15}	angular frequency of seed laser
ω_s (rad/s)	4.82×10^{15}	angular frequency of pump laser
Δ_2 (rad/s)	6.67×10^{14}	detuning $\omega_p - 2\pi c/\lambda_{21}$
Δ_3 (rad/s)	3.05×10^{14}	detuning $\omega_p - 2\pi c/\lambda_{31}$
Δ_4 (rad/s)	-4.04×10^{13}	detuning $\omega_p - 2\pi c/\lambda_{41}$
Δ_5^p (rad/s)	-2.46×10^{15}	detuning $\omega_p - 2\pi c/\lambda_{51}$
Δ_5^s (rad/s)	0	detuning $\omega_s - 2\pi c/\lambda_{51}$
τ (fs)	20	pulse duration of laser pulse
W_0 (Hz)	1.78927×10^{19}	tunnelling ionization rate
ρ_{ii}	based on simulation	population of state $ i\rangle$
ρ_{ij}	based on simulation	coherence between state $ i\rangle$ and $ j\rangle$ ($i \neq j$)
$E_{p(s)}$ (V/m)	based on simulation	electric field of pump (seed) laser
$\Omega_{p(s)}$ (rad/s)	$P_{A(B)}E_{p(s)}/\hbar$	Rabi frequency of pump(seed) laser
Ω_f (rad/s)	$P_B E_p/\hbar$	Rabi frequency of pump laser driving transition $ 1\rangle \rightarrow 5\rangle$
ω_2 (rad/s)	1.7×10^{15}	$ 1\rangle \rightarrow 2\rangle$ transition angular frequency
ω_3 (rad/s)	4.82×10^{15}	$ 1\rangle \rightarrow 5\rangle$ transition angular frequency
v_1 (rad/s)	3.51×10^{14}	$ 2\rangle \rightarrow 3\rangle$ transition angular frequency
v_2 (rad/s)	6.97×10^{14}	$ 2\rangle \rightarrow 4\rangle$ transition angular frequency

Appendix B: The determination of branching ratio F_{ii}

We use the ab initio potential of neutral N_2 and N_2^+ cation [16] to solve the vibrational Schrödinger equation in the discrete variable representation (DVR)[28]. The potential curves of the electronic ground state $X^1\Sigma_g^+$ of N_2 molecule and the $X^2\Sigma_g^+$, $A^2\Pi_u$ and $B^2\Sigma_u^+$ ($\nu = 0$) states of N_2^+ cation are shown in Fig. 7. In the discrete variable representation, the Hamiltonian matrix elements are written as[28]

$$H_{ii'} = \begin{cases} \frac{(-1)^{i-i'}}{2\Delta x^2} \frac{\pi^2}{3} + V(x_i), & i = i' \\ \frac{(-1)^{i-i'}}{2\Delta x^2} \frac{2}{(i-i')}, & i \neq i' \end{cases} \quad (\text{B1})$$

We then solve the Schrödinger's equation to get the branching ratios F_{ii} , which are defined as

$$\begin{aligned} F_{ii}^A &= |\langle \phi_{vi}(A(N_2^+)) | \psi_0(X(N_2)) \rangle|^2 \\ F_{ii}^B &= |\langle \phi_{vi}(B(N_2^+)) | \psi_0(X(N_2)) \rangle|^2. \end{aligned} \quad (\text{B2})$$

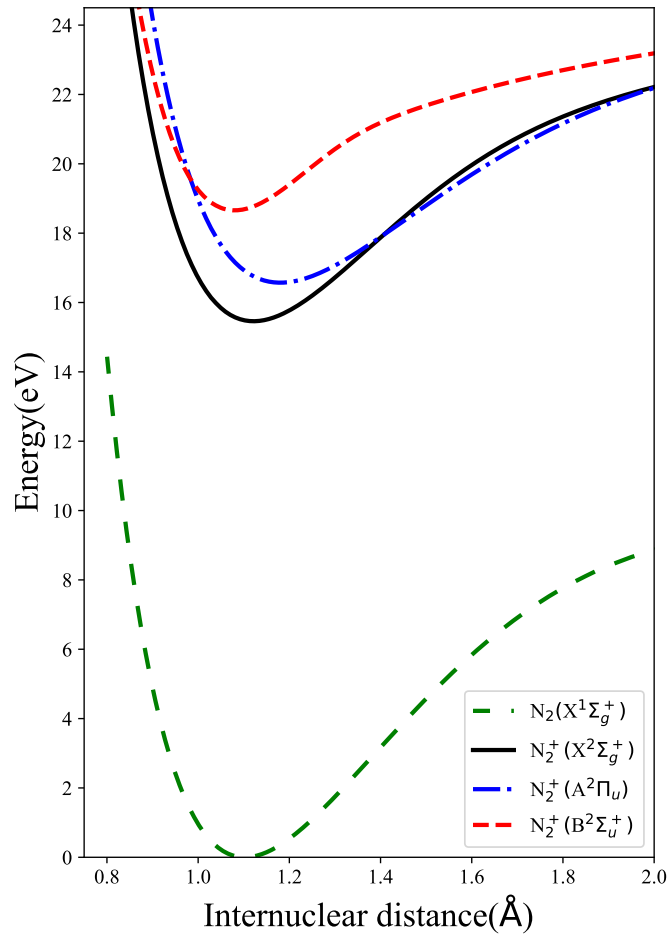


FIG. 7: Potential energy curves of the electronic ground state $X^1\Sigma_g^+$ of N_2 molecule and the $X^2\Sigma_g^+$, $A^2\Pi_u$ and $B^2\Sigma_u^+$ ($\nu = 0$) states of N_2^+ cation.[16].

[1] J. Yao, B. Zeng, H. Xu, G. Li, W. Chu, J. Ni, H. Zhang, S. L. Chin, Y. Cheng, and Z. Xu, Phys. Rev. A **84**, 051802 (2011).

[2] Y. Liu, P. Ding, G. Lambert, A. Houard, V. Tikhonchuk, and

- A. Mysyrowicz, Phys. Rev. Lett. **115**, 133203 (2015).
- [3] Y. Liu, P. Ding, N. Ibrakovic, S. Bengtsson, S. Chen, R. Danylo, E. R. Simpson, E. W. Larsen, X. Zhang, Z. Fan, et al., Phys. Rev. Lett. **119**, 203205 (2017).
- [4] H. Xu, E. Lötstedt, A. Iwasaki, and K. Yamanouchi, Nature Commun. **6**, 8347 (2015).
- [5] A. Azarm, P. Corkum, and P. Polynkin, Phys. Rev. A **96**, 051401 (2017).
- [6] M. Britton, P. Laferrere, D. H. Ko, Z. Li, F. Kong, G. Brown, A. Naumov, C. Zhang, L. Arissian, and P. B. Corkum, Phys. Rev. Lett. **120**, 133208 (2018).
- [7] W. Zheng, Z. Miao, L. Zhang, Y. Wang, C. Dai, A. Zhang, H. Jiang, Q. Gong, and C. Wu, J. Phys. Chem. Lett. **10**, 6598 (2019).
- [8] J. Chen, J. Yao, H. Zhang, Z. Liu, B. Xu, W. Chu, L. Qiao, Z. Wang, J. Fatome, O. Faucher, et al., Phys. Rev. A **100**, 031402(R) (2019).
- [9] H. Li, M. Hou, H. Zang, Y. Fu, E. Lötstedt, T. Ando, A. Iwasaki, K. Yamanouchi, and H. Xu, Phys. Rev. Lett. **122** (2019).
- [10] J. Yao, W. Chu, Z. Liu, J. Chen, B. Xu, and Y. Cheng, Appl. Phys. B **124**, 1 (2018).
- [11] J. Yao, W. Chu, Z. Liu, B. Xu, J. Chen, and Y. Cheng, New J. Phys. **20**, 33035 (2018).
- [12] Z. Liu, J. Yao, J. Chen, B. Xu, W. Chu, and Y. Cheng, Phys. Rev. Lett. **120**, 083205 (2018).
- [13] T. Ando, E. Lötstedt, A. Iwasaki, H. Li, Y. Fu, S. Wang, H. Xu, and K. Yamanouchi, Phys. Rev. Lett. **123**, 203201 (2019).
- [14] A. Zhang, Q. Liang, M. Lei, L. Yuan, Y. Liu, Z. Fan, X. Zhang, S. Zhuang, C. Wu, Q. Gong, et al., Opt. Express **27**, 12638 (2019).
- [15] A. Zhang, M. Lei, J. Gao, C. Wu, Q. Gong, and H. Jiang, Opt. Express **27**, 14922 (2019).
- [16] J. Yao, S. Jiang, W. Chu, B. Zeng, C. Wu, R. Lu, Z. Li, H. Xie, G. Li, C. Yu, et al., Phys. Rev. Lett. **116**, 143007 (2016).
- [17] G. Grynberg, A. Aspect, and C. Fabre, *Introduction to Quantum Optics: From the Semi-classical Approach to Quantized Light* (Cambridge University Press, 2010), ISBN 0521551129.
- [18] J. C. MacGillivray and M. S. Feld, Phys. Rev. A **14**, 1169 (1976).
- [19] L. Yuan and A. A. Svidzinsky, Phys. Rev. A **85**, 033836 (2012).
- [20] C. Weninger and N. Rohringer, Phys. Rev. A **90**, 063828 (2014).
- [21] F. T. Arecchi and E. Courtens, Phys. Rev. A **2**, 1730 (1970).
- [22] D. Polder, M. F. H. Schuurmans, and Q. H. F. Vreken, Phys. Rev. A **19**, 1192 (1979).
- [23] M. Schuurmans and D. Polder, Phys. Lett. A **72**, 306 (1979).
- [24] M. V. Ammosov, Sov. Phys. JETP **64**, 1191 (1987).
- [25] J. M. Lilly and S. C. Olhede, IEEE Trans. Signal Process. **57**, 146 (2008).
- [26] M. D. Crisp, Phys. Rev. A **1**, 1604 (1970).
- [27] M. O. Scully and M. S. Zubairy, *Quantum Optics* (Cambridge University Press, 2006).
- [28] D. T. Colbert and W. H. Miller, J. Chem. Phys. **96**, 1982 (1992).